The manuscript is published in Soil and Foundations 2017, 57(3): 371-383
DOI: https://doi.org/10.1016/j.sandf.2017.05.005

An elastoplastic model for hydro-mechanical behavior of unsaturated soils

H. Ghasemzadeh[1], M.H. Sojoudi[2*], S.A. Ghoreishian Amiri[1,3], M.H. Karami[2]

[1]Faculty of Civil Engineering, K. N. Toosi University of Technology, Tehran, Iran.
[2]Faculty of Engineering, Shahed University, Tehran, Iran.
[3]Norwegian University of Science and Technology (NTNU), Trondheim, Norway.

Abstract

A coupled elastoplastic constitutive model is presented for describing the hydraulic and mechanical behavior of unsaturated soils. The model is capable of considering the influence of irreversible changes in water saturation on the mechanical behavior and plastic deformation on hydraulic behavior. The mechanical and hydraulic behaviors are captured using the subloading surface and bounding surface plasticity frameworks, respectively. The coupling between hydraulic and mechanical behaviors is established using intergranular stress concept in addition to appropriate coupled hardening rules. Attention is also given to the movement of soil water characteristic curve due to the plastic deformation. Model predictions for some unsaturated soil samples are compared with experimental data, and reasonable agreement is achieved.

Keywords: unsaturated soil, plasticity, hydro-mechanical coupling, bounding surface, subloading surface.

1. Introduction

Constitutive modeling of hydraulic and mechanical behavior of unsaturated soils is a subject of great interest in geotechnical engineering practice. The influence of degree of saturation on mechanical behavior and the influence of volumetric strain on hydraulic behavior are now demonstrated with experiments (e.g. [1]). The description of the hydro-mechanical behavior of unsaturated soils with the identification of the

* Corresponding author Email: mh.sojoudi@shahed.ac.ir

coupled influences of hydraulic and mechanical behaviors has been a key area of research in modern geomechanics.

Although several constitutive models for unsaturated soils have been proposed over the last two decades (e.g. [2-16]), many fundamental issues such as the selection of stress-strain variables and the framework of hydro-mechanical coupling are still under debate. After the pioneering work of Alonso et al. [2], two stress-state variables concept with net stress and matric suction have been widely used to describe the hydro-mechanical behavior of unsaturated soils [8, 17-20]. However, Wheeler [21], Sharma [1] and Sun et al. [22] demonstrated that some fundamental coupling effects of hydraulic and mechanical behaviors cannot be captured by the use of net stress and matric suction.

Wheeler and his colleagues [7] employed Bishop's effective stress and modified suction as the stress-state variables to simulate the coupled influences of degree of saturation and volumetric deformation on mechanical and hydraulic behavior of unsaturated soils, respectively. The model proposed by Wheeler et al. [7] is restricted to isotropic loading conditions. Sheng et al. [9] and Sun et al. [10] extended Wheeler et al.'s model to deviatoric loading condition. However, it seems that they placed more emphasis on the influence of hydraulic behavior on the stress-strain relation, and paid less attention on the influence of deformation on hydraulic behavior.

Recently, Muraleetharan et al. [23] proceeded to use intergranular stress tensor and matric suction as the stress-state variables to improve Wheeler et al.'s [7] framework. Although this model could properly simulate problems with multiple cycles of wetting and drying, its capability for simulating problems those involve multiple cycles of mechanical loading and unloading is under debate. Ghasemzadeh and Ghoreishian Amiri [24] extended Muraleetharan et al.'s framework to represent a more realistic model for simulating the coupled hydro-mechanical behavior of unsaturated soils. The model is capable of considering the influence of the water volume fraction on mechanical behavior, such as irreversible compression during the drying path that do not exceed the maximum value of suction previously

experienced by the soil, and the coupling effects on the reverse direction, as well as the variation of the water volume fraction due to mechanical loading or unloading. However, these two models are restricted to isotropic stress states.

Liu and Muraleetharan [25, 26] extended Muraleetharan et al.'s model [23] for general stress states. The model could successfully capture the mechanical behavior of unsaturated soil under complex mechanical loading conditions. However, assuming fixed wetting and drying bounding curves in suction-volumetric water content space, the model can't successfully simulate the effects of plastic deformation on the hydraulic behavior of the samples involving a reduction of suction as a result of plastic compression. Moreover, the model is restricted to unsaturated silts and sands.

The main objective of this paper is to present a comprehensive, fully coupled hydro-mechanical elastoplastic constitutive model for a wide range of unsaturated soils from silts to collapsible and highly expansive clays. The work is an extension of the model proposed by Ghasemzadeh and Ghoreishian Amiri [24], covering anisotropic loading conditions. The method of calibration is also described and the capability of the model for capturing the coupled hydro-mechanical behavior of unsaturated soils are verified using many laboratory test results.

Note that throughout this paper, compressive stress and strain are assumed to be positive.

2. Hydro-mechanical elastoplastic framework

It is assumed that the water volume fraction and strain increments (dn_w and $d\boldsymbol{\varepsilon}$) are additively decomposed into elastic and plastic parts:

$$d\boldsymbol{\varepsilon} = d\boldsymbol{\varepsilon}^e + d\boldsymbol{\varepsilon}^p \tag{1}$$

$$dn_w = dn_w^e + dn_w^p \tag{2}$$

where the water volume fraction is defined as the ratio of the volume of water (v_w) over the total volume

of soil (v):

$$n_w = \frac{v_w}{v} \tag{3}$$

The selection of appropriate stress and strain variables is an essential step for developing constitutive models for unsaturated soils. As thermodynamically demonstrated by Wei [27] and successfully used by other researchers [23-26], the intergranular stress tensor $(\boldsymbol{\sigma}^*)$, the matric suction (s), the plastic strain $(d\varepsilon^p)$ and the irrecoverable part of the water volume fraction (dn_w^p) can be selected as the conjugated stress-strain variables. The intergranular stress tensor is defined as:

$$\boldsymbol{\sigma}^* = \boldsymbol{\sigma}_{net} + \chi s\, \mathbf{I} \qquad \begin{cases} \chi = n_w & \text{for unsaturated state} \\ \chi = 1 & \text{for saturated state} \end{cases} \tag{4}$$

where $\mathbf{I}$ is the unit tensor, and $\boldsymbol{\sigma}_{net}$ is the net stress tensor. In equation (4), the intergranular stress tensor should cover the Terzaghi's effective stress in fully saturated condition. It means that a switch is required between the saturated and unsaturated states. However, since the value of suction at the moment of transition between saturated and unsaturated conditions is equal to zero, the effective stress and intergranular stress will not be affected by the value of χ, and thus, the transition between saturated and unsaturated states can be performed without any problem [23].

Based on the work presented by Ghasemzadeh and Ghoreishian Amiri [24], the process of slippage, widening and closing between granular medium particles is simulated by introducing a Loading Collapse (LC) normal yield surface (as later defined) within the framework of subloading surface plasticity [28, 29]. However, the bounding surface plasticity framework [30, 31] is employed to capturing the Soil Water Characteristic Curves (SWCCs) which is associated with Suction Decreased (SD) and Suction Increased (SI) bounding surfaces (as later defined). The superiority of employing the subloading and bounding surface frameworks in contrast with the traditional plasticity frameworks is completely discussed by Ghasemzadeh

and Ghoreishian Amiri [24]. Figure 1 shows the forms and evolutions of SI, SD bounding and LC normal yield curves in isotropic stress space. It is worth noting that according to the argument discussed by Wheeler et al. [7], the shapes of SI and SD bounding and LC normal yield curves, in the isotropic stress space, are assumed straight lines.

Figure 2 shows the LC normal yield and subloading surfaces in $p^* - q$ plane. The complete view of SI and SD bounding and LC normal yield surfaces for a triaxial stress state are shown in figure 3.

3. Model formulation

As mentioned earlier, the subloading surface and bounding surface plasticity frameworks are employed to describe the mechanical and hydraulic behaviors, respectively. Full coupling of the hydraulic and mechanical behaviors is achieved by introducing appropriate coupled hardening rules.

3.1. Bounding surfaces

The normal yield surface and bounding surfaces are described by the following functions:

$$f(\boldsymbol{\sigma}_y^*) = p_y^* + \frac{2{q_y}^2}{3m^2 p_y^*} = F(H) \tag{5}$$

$$s = s_{I0} \tag{6}$$

$$s = s_{D0} \tag{7}$$

where s_{I0} and s_{D0} introduce the position of the SI and SD bounding surfaces, respectively. $\boldsymbol{\sigma}_y^*$ ($= \begin{bmatrix} p_y^* & q_y \end{bmatrix}^T$) introduces the stress states on the LC normal yield surface, m is the slope of the critical state line in $q - p^*$ plane (q: deviatoric stress), and F introduces the position/size of the surface and is a function of the isotropic hardening variable (H) [29]:

$$F = F_0 \exp(\frac{H}{\lambda_S - K}) \tag{8}$$

where F_0 is the initial value of F, λ_S and K are the slopes of the normal consolidation and swelling lines in $\ln v - \ln p^*$ space (v is the specific volume), respectively. The initial value of F depends on the maximum value of pressure previously experienced by the soil and must be introduced as a calibration parameter. The isotropic hardening variable (H) will be defined later in section 3.2.

Using experiments, Liu and Muraleetharan [32] reported that all scanning curves of SWCCs are bounded by primary wetting and secondary drying curves (figure 4). These curves describe the initial values and evolution rules of s_{D0} and s_{I0}. If the soil starts from an oven dried state and is then subjected to wetting, it will follow the primary wetting curve. If wetting is continued until the saturated state, and is then subjected to drying, the soil will follow the secondary drying curve. Feng and Fredlund [33] proposed two mathematical equations to describe these two curves in $s - n_w$ space:

$$s_{D0} = b_1 [\frac{n_{w_{sat}} - n_w}{n_w - n_{w_{res}}}]^{\frac{1}{d_1}} \tag{9}$$

$$s_{I0} = b_2 [\frac{n_{w_{sat}} - n_w}{n_w - n_{w_{res}}}]^{\frac{1}{d_2}} \tag{10}$$

where $n_{w_{sat}}$ and $n_{w_{res}}$ are the values of the water volume fraction at zero and very high suction, respectively. b_1, d_1, b_2 and d_2 are four material parameters that describe the primary wetting and secondary drying curves in the $s - n_w$ space. It should be noted that the saturation state of the soil, in equations (9) and (10), will be reached only when the value of suction equals zero. It means that the saturation state of the soil corresponding to the values of suction lower than air entry value is not considered in these equations.

3.2. Coupled hardening rules

As mentioned in the previous section, the position of the LC normal yield surface is controlled by the function F. Therefore, the movement of this surface can be formulated by differentiating equation (8):

$$dF = \frac{F_0}{\lambda_S - K}\exp(\frac{H}{\lambda_S - K})dH = F'dH \tag{11}$$

where, the coupled evolution rule of the isotropic hardening variable, H, could be introduced as:

$$dH = d\varepsilon_v^p - dn_w^p \tag{12}$$

Following the argument discussed by Ghasemzadeh and Ghoreishian Amiri [24], the plastic part of compression and expansion causes the primary wetting and secondary drying curves to move right and left in the $s - n_w$ plane. The possible movement of these curves due to plastic compression is schematically shown in Figure 5. This could be captured by the following hardening rules [24]:

$$dn_{w_{res}} = \alpha_1 n_w d\varepsilon_v^p \tag{13}$$

$$dn_{w_{sat}} = \alpha_2 n_w d\varepsilon_v^p \tag{14}$$

where α_1 and α_2 are two material parameters which control the movement of primary wetting and secondary drying curves due to plastic volumetric strain [24]. It is worth noting that the initial values of $n_{w_{sat}}$ and $n_{w_{res}}$ should also be considered as material parameters.

The last hardening rules should control the movement of the SD and SI bounding curves with respect to the fact that the values of s_{D0} and s_{I0} must always lie on the primary wetting and secondary drying curves.

Therefore, the new position of s_{D0} and s_{I0} (at the end of load step n) can be found by replacing the new values of n_w, $n_{w_{sat}}$ and $n_{w_{res}}$ in equations (9) and (10):

$$\left(s_{D0}\right)_{n+1} = b_1 \left[\frac{\left(n_{w_{sat}}\right)_n - \left(n_w\right)_n}{\left(n_w\right)_n - \left(n_{w_{res}}\right)_n} \right]^{\frac{1}{d_1}} \tag{15}$$

$$\left(s_{I0}\right)_{n+1} = b_2 \left[\frac{\left(n_{w_{sat}}\right)_n - \left(n_w\right)_n}{\left(n_w\right)_n - \left(n_{w_{res}}\right)_n} \right]^{\frac{1}{d_2}} \tag{16}$$

Note that variation of s_{D0} and s_{I0} due to elastic deformation is neglected.

3.3. Elastoplastic calculations

The elastic evolution of the mechanical strain and the water volume fraction are described as follows:

$$d\varepsilon_v^e = \frac{k dp^*}{\nu p^*} \quad \left(\text{where} \quad \varepsilon_v = \varepsilon_x + \varepsilon_y + \varepsilon_z\right) \tag{17}$$

$$d\varepsilon_q^e = \frac{dq}{2G} \quad \left(\text{where} \quad \varepsilon_q = \sqrt{\frac{1}{2}\left[(\varepsilon_x - \varepsilon_y)^2 + (\varepsilon_x - \varepsilon_z)^2 + (\varepsilon_z - \varepsilon_y)^2 + \frac{3}{4}(\gamma_{xy}^2 + \gamma_{xz}^2 + \gamma_{yz}^2) \right]} \right) \tag{18}$$

$$dn_w^e = \frac{ds}{\Gamma^e} \tag{19}$$

where ε_v^e and ε_q^e are the elastic volumetric and deviatoric strains, respectively, γ_{ij} denotes the engineering shear strain, k is the slope of the elastic swelling line in $\nu - \ln p^*$ plane, G is the shear elastic modulus and Γ^e is the elastic capillary modulus. The specific volume, ν, and shear modulus, G, are defined as:

$$\nu = \frac{1}{1-n} \tag{20}$$

$$G = \frac{3p^*(1-2\upsilon)}{2K(1+\upsilon)} \tag{21}$$

where n is the porosity, υ is the Poisson's ratio and K has been previously defined in equation (8).

As mentioned earlier, in this model the plastic deformation is calculated within the subloading surface elastoplasticity framework. It should be mentioned that the LC normal yield surface is the renamed form of the conventional LC yield surface, while its interior is not regarded as a purely elastic domain. Indeed, in this framework, in addition to the LC normal yield surface, we need to introduce the subloading surface. The subloading surface is defined as a surface which always passes through the current stress point, while keeping a similar shape to the LC normal yield surface with respect to the origin of the stress space:

$$f(\boldsymbol{\sigma}^*) = p^* + \frac{2q^2}{3m^2 p^*} = RF(H) \tag{22}$$

where R is the similarity ratio of the subloading surface to the LC normal yield surface. This ratio is called the normal yield ratio. Differentiating equation (22) results in:

$$\left(\frac{\partial f(\boldsymbol{\sigma}^*)}{\partial \boldsymbol{\sigma}^*}\right)^T d\boldsymbol{\sigma}^* = FdR + RF'dH \tag{23}$$

The evolution of the normal yield ratio could be described as [29]:

$$dR = U\left\|d\varepsilon^p\right\| \text{ for } d\varepsilon^p \neq 0 \tag{24}$$

where *U* is a monotonically decreasing function of *R* that should satisfy the following conditions:

$$
\begin{aligned}
&U = +\infty \text{ for } R = 0 \\
&U = 0 \quad \text{for } R = 1 \\
&U < 0 \quad \text{for } R > 1
\end{aligned}
\tag{25}
$$

These conditions are required to guarantee that the subloading surface approaches the normal yield surface during a loading process. The equation satisfying conditions (25) is described by Hashigushi et al. [29]:

$$
U = -u \ln R \tag{26}
$$

where u is a material parameter. Substituting equations (12) and (24) into equation (23), one obtains:

$$
\left(\frac{\partial f(\boldsymbol{\sigma}^*)}{\partial \boldsymbol{\sigma}^*} \right)^T d\boldsymbol{\sigma}^* = U \left\| d\boldsymbol{\varepsilon}^p \right\| F + RF'(d\varepsilon_v^p - dn_w^p) \tag{27}
$$

Assuming the associated flow rule:

$$
d\boldsymbol{\varepsilon}^p = \lambda \bar{\mathbf{N}} \tag{28}
$$

where λ is the positive proportionality factor, and the vector $\bar{\boldsymbol{N}}$ is the unit normal vector of the subloading surface at the current stress point:

$$
\bar{\mathbf{N}} = \frac{\partial f(\boldsymbol{\sigma}^*)}{\partial \boldsymbol{\sigma}^*} \Bigg/ \left\| \frac{\partial f(\boldsymbol{\sigma}^*)}{\partial \boldsymbol{\sigma}^*} \right\| \tag{29}
$$

Substituting equation (28) into equation (27) leads to:

$$
\lambda = \frac{\bar{\mathbf{N}}^T d\boldsymbol{\sigma}^*}{M^P} + \frac{dn_w^p}{L^P} \tag{30}
$$

where

$$M^P = \left(\frac{U}{R} + \frac{F'}{F}\bar{h}\right).\left(\bar{\mathbf{N}}^T\boldsymbol{\sigma}^*\right) \tag{31}$$

$$L^P = \frac{U.F}{R.F'} + \bar{h} \tag{32}$$

$$\bar{h} = \frac{\partial f(\boldsymbol{\sigma}^*)}{\partial p^*} \Bigg/ \left\| \frac{\partial f(\boldsymbol{\sigma}^*)}{\partial \boldsymbol{\sigma}^*} \right\| \tag{33}$$

$$d\boldsymbol{\varepsilon}^p = \begin{pmatrix} d\varepsilon_v^p \\ d\varepsilon_q^p \end{pmatrix} \tag{34}$$

$$d\boldsymbol{\sigma}^* = \begin{pmatrix} dp^* \\ dq \end{pmatrix} \tag{35}$$

The plastic strain increment can now be calculated from equations (28) and (30):

$$d\boldsymbol{\varepsilon}^p = \frac{\bar{\mathbf{N}}^T}{M^P}\left(d\boldsymbol{\sigma}^*\right)\bar{\mathbf{N}} + \frac{dn_w^p}{L^P}\bar{\mathbf{N}} \tag{36}$$

Equation (36) reveals that the plastic strain increment consists of two parts: the mechanical part ($\frac{\bar{\mathbf{N}}^T}{M^P}(d\boldsymbol{\sigma}^*)\bar{\mathbf{N}}$), which is the result of the integranular stress increment, and the hydraulic part ($\frac{dn_w^p}{L^P}\bar{\mathbf{N}}$), which comes from the variation of the irrecoverable part of water volume fraction. Consequently, the plastic strain components can be decomposed as:

$$d\varepsilon_v^p = d\varepsilon_{vm}^p + d\varepsilon_{vh}^p \tag{37}$$

$$d\varepsilon_q^p = d\varepsilon_{qm}^p + d\varepsilon_{qh}^p \tag{38}$$

where $d\varepsilon_{vm}^{p}$ and $d\varepsilon_{vh}^{p}$ are the mechanical and hydraulic parts of the plastic volumetric strain increment, respectively; $d\varepsilon_{qm}^{p}$ and $d\varepsilon_{qh}^{p}$ are the mechanical and hydraulic parts of the plastic deviatoric strain increment, respectively.

Based on the loading criterion proposed by Hashiguchi et al. [29], the loading criterion in the proposed model is given by:

$$\begin{aligned}
&(\frac{\partial f(\boldsymbol{\sigma}^{*})}{\partial p^{*}}\frac{v.p^{*}}{k}).d\varepsilon_{v}+(\frac{\partial f(\boldsymbol{\sigma}^{*})}{\partial q}.2\mathrm{G}).d\varepsilon_{q}>0\rightarrow d\boldsymbol{\varepsilon}^{p}\neq 0\\
&(\frac{\partial f(\boldsymbol{\sigma}^{*})}{\partial p^{*}}\frac{v.p^{*}}{k}).d\varepsilon_{v}+(\frac{\partial f(\boldsymbol{\sigma}^{*})}{\partial q}.2\mathrm{G}).d\varepsilon_{q}\leq 0\rightarrow d\boldsymbol{\varepsilon}^{p}=0
\end{aligned} \tag{39}$$

According to Ghasemzadeh and Ghoreishian Amiri [24], the plastic part of the water volume fraction can be calculated as:

$$dn_{w}^{p}=\frac{ds}{\Gamma^{p}}+\left(\frac{\bar{\mathbf{N}}^{T}}{M^{P}}\left(d\boldsymbol{\sigma}^{*}\right)\bar{h}\right).n_{w} \tag{40}$$

where Γ^{p} is the plastic capillary modulus which can be calculated in the bounding surface plasticity framework [30, 31]:

$$\Gamma^{p}=\Gamma_{0}^{p}(1+\frac{h.\delta}{\langle\delta_{in}-g\delta\rangle}) \tag{41}$$

where h and g are material parameters, $\langle\rangle$ are Macaulay brackets, δ is the vertical distance of the current stress state point to the SD or SI bounding curves in the wetting or drying process (figure 6), δ_{in} is the value of δ at the beginning of each wetting/drying path and Γ_{0}^{p} is the value of Γ^{p} at $\delta=0$ which is calculated as:

$$\Gamma_0^p = \frac{ds_{D0}}{dn_w^p} \text{ in wetting path} \tag{42}$$

$$\Gamma_0^p = \frac{ds_{I0}}{dn_w^p} \text{ in drying path} \tag{43}$$

It is worth noting, $\delta = \delta_{in}$ in equation (41) means elastic behavior dominates $(\Gamma^p = \infty)$ which occurs at the beginning of each wetting or drying path. In the other case, when $\delta = 0$ the plastic capillary modulus is equal to zero ($\Gamma^p = 0$) which means that the stress state lies on the corresponding bounding curve.

4. Comparison with experiments

The ability of the model in simulating the hydro-mechanical behavior of unsaturated Pearl clay and a bentonite-kaolin mixture under isotropic loading conditions was presented in [24]. In this paper, to examine the ability of the extended version of the model against anisotropic loading conditions, experimental results using Pearl clay [34], compacted speswhite kaolin [35, 36] and Bourke silt [37] are compared with model predictions.

Pearl clay behaves like collapsible soils which consist of weak materials. This kind of soil compacts and collapses under the excessive loading or addition of water. On the other hand, compacted speswhite kaolin and bentonite–kaolin mixtures behave as moderately and highly expansive soils, respectively.

4.1. Determination of material parameters

In the proposed model, seven stress-strain parameters (F_0, u, k, m, λ_s, K and υ), nine hydraulic parameters (b_1, d_1, b_2, d_2, Γ^e, h, g, $n_{w_{sat}}$ and $n_{w_{res}}$) and two coupling parameters (α_1, α_2) are required. A common drained shear stress test at the saturated state of the soil can be used for determining the Poisson's ratio (υ) and the slope of the critical state line (m). The parameters F_0, λ_s, K and κ which respectively indicate the pre-consolidation pressure, the slope of the normal consolidation line in

$\ln\nu - \ln p^*$ plane and the slopes of swelling lines in $\ln\nu - \ln p^*$ and $\nu - \ln p^*$ planes, can be determined using an isotropic drained compression test at the saturated state of the soil. The parameter u does not have a clear physical meaning and mathematically stands to adjust the curvature of the stress–strain diagram. This parameter can be found by a trial-and-error procedure to fit the curvature of the soil behavior in its transitional state in stress- strain space.

The initial values of $n_{w_{sat}}$ and $n_{w_{res}}$ can be determined from the maximum and minimum value of n_w at the primary wetting and secondary drying curves, respectively. The values of b_1, d_1 and b_2, d_2 can be determined by conducting a curve-fitting procedure on primary wetting and secondary drying curves using equations (9) and (10), respectively. The values of Γ^e, h and g may be found by a trial-and-error procedure using the scanning curve data from laboratory tests. It is worth noting that since the specific volume varies during the experimental measurement of SWCCs, the initial values of $n_{w_{sat}}$ and $n_{w_{res}}$, which has been determined by the maximum and minimum value of n_w at the primary wetting and secondary drying curves, do not correspond to the initial specific volume. Therefore, in order to accurately reproduce the primary wetting and secondary drying curves, some modifications on the initial values of $n_{w_{sat}}$ and $n_{w_{res}}$ are required to fit the computed curves with those obtained by laboratory.

The coupling parameters α_1 and α_2 can be found using the variation of the primary wetting and secondary drying curves of the soil after a cycle of isotropic loading-unloading. After this cycle, some plastic deformation will remain in the sample. Considering the value of the remained plastic strain and the variation of $n_{w_{sat}}$ and $n_{w_{res}}$ after this loading-unloading cycle, α_1 and α_2 can be found using equations (13) and (14). It is worth noting that since equations (13) and (14) describe nonlinear relations between hydraulic behavior and plastic strain variation, a trial-and-error procedure by simulating the above-mentioned test is highly recommended.

4.2. Pearl clay

Sun et al. [34] reported the results of some triaxial and isotropic loading tests on samples of Pearl clay with 50% silt and 50% clay. The samples, which was prepared and used for the tests, had a liquid limit of 49, a plasticity index of 22 and a specific gravity of 2.71. The samples were prepared by compaction in a mould at a water content of about 26 %. The material parameters that are used to predict the soil behavior are listed in table 1.

The comparison of test data and model results for a triaxial extension test with a constant mean net stress of 196 kPa and an imposed wetting path at a stress ratio (σ_r / σ_a) of about 2.2, is presented in figure 7. The initial values of n_w and n at the beginning of the test are 0.347and 0.57, respectively. The stress path for this test involved three following phases:

Phase 1:: constant matric suction: 147 kPa ; deviatoric stress: $0 \rightarrow 166$ kPa

Phase 2:: matric suction 147 kPa $\rightarrow 0$; constant deviatoric stress: 166 kPa

Phase 3:: constant matric suction: 0; deviatoric stress: 166 kPa $\rightarrow 300$ kPa

Figure 8 shows the sensitivity of the stress-strain curves to different values of coupling parameters (α_1 and α_2). As shown in the figure, the initial part of the results is not highly affected by the coupling parameters, but imposing the wetting path activates the effects of these parameters, since the hydraulic part of the plastic strains are highly affected by the positions of $n_{w_{sat}}$ and $n_{w_{res}}$.

Figure 9 shows the comparisons of the predicted and measured results of a triaxial compression test with constant mean net stress ($p = 196$ kPa) and constant suction ($s = 147$ kPa). The values of n_w and n at the beginning of the test are 0.312 and 0.57, respectively.

Figure 10 shows the test results and model predictions for a one-dimensional collapse test. The initial values of n_w and n at the beginning of the test are 0.308 and 0.57, respectively. The stress path in this test involved three different phases:

Phase 1:: Suction: $140\ \text{kPa} \rightarrow 147\ \text{kPa}$, Constant mean net stress: $20\ \text{kPa}$

Phase 2:: Constant suction: $147\ \text{kPa}$, Mean net stress: $20\ \text{kPa} \rightarrow 196\ \text{kPa}$

Phase 3:: Suction: $147\ \text{kPa} \rightarrow 0$, Constant mean net stress: $196\ \text{kPa}$

Figure 11 shows the comparison of measured results and model predictions for another collapse test on Pearl clay. The initial conditions for this test are the same as for the previous test. This test was conducted under the following loading phases:

Phase 1:: Suction: $140\ \text{kPa} \rightarrow 245\ \text{kPa}$, Constant mean net stress: $16.11\ \text{kPa}$

Phase 2:: Constant suction: $245\ \text{kPa}$, Mean net stress: $16.11\ \text{kPa} \rightarrow 45\ \text{kPa}$

Phase 3:: Suction: $245\ \text{kPa} \rightarrow 0$, Constant mean net stress: $45\ \text{kPa}$

Phase 4:: Constant suction: 0, Mean net stress: $45\ \text{kPa} \rightarrow 597\ \text{kPa}$

Phase 5:: Constant suction: 0, Mean net stress: $597\ \text{kPa} \rightarrow 210\ \text{kPa}$

4.3. Compacted speswhite kaolin

The experimental results on compacted speswhite kaolin under triaxial loading states are reported by Wheeler and Sivakumar [35, 36]. The samples were prepared by compacting the mix of dry speswhite kaolin powder and water in a mould. Prior to compacting, the larger clods of soil in the wet mix were broken up with a pestle and mortar, and the material then sieved through a 1.12 mm aperture sieve. The model parameters for simulating the behavior of speswhite kaolin by the proposed model are listed in table 2.

Figure 12 shows the test results and model predictions for a drained triaxial compression test on a saturated speswhite kaolin sample. The initial values of mean net stress and n are 150 kPa and 0.5, respectively.

Figures13 and 14 show the comparison of the model results and experimental data for two unsaturated states of the soil with the constant suction of 100 and 300 kPa, respectively. The initial conditions of these tests are the same as for the previous one.

The ability of the model to simulate the behavior of a soil in saturated and unsaturated conditions with a single set of material parameters is validated in this section.

4.4. Bourke silt

Uchaipichat [37] reported a set of triaxial tests on unsaturated Bourke silt with a liquid limit of 20.5, a plasticity index of 14.5 and a specific gravity of 2.65. The samples were statically compacted to a dry unit weight of about 15.3 kN/m^3, at a moisture content of 10.5%. The samples were prepared dry of optimum to obtain a soil matrix amenable to stiffening with the increasing matric suction. The material parameters for this soil are listed in table 3.

Figures 15-17 show three sets of drained triaxial tests with the constant cell pressure of 150 kPa. The first test is done on a saturated sample, whereas, the value of suction for the others are kept constant at 100 and 300 kPa. The initial values of n_w and n for the sample in saturated condition are 0.511, for the test with the suction value of 100 kPa are considered to be 0.3 and 0.514, respectively, and for the test with the suction value of 300 kPa are set to 0.2 and 0.516.

The results show the ability of the proposed model in the simulation of the hydro-mechanical behavior of saturated and unsaturated silts as well as clays. Modeling this range of soils in unified constitutive equations could be mentioned as the superiority of the proposed model in contrast with previous ones.

Concluding remarks

In this paper an elastoplastic constitutive model based on the two stress state variables approach is presented to describe the coupled hydro-mechanical behavior of unsaturated soils. The employed stress variables are intergranular stress and matric suction, which are conjugated with the conventional strain increment and the increment of the water volume fraction, respectively.

In the proposed model, subloading surface and bounding surface plasticity frameworks are employed to describe the mechanical and hydraulic behavior, respectively. Since there are no purely elastic domains in the selected frameworks, the proposed model fulfills the smoothness condition, and thus, the smooth elastic-plastic transition is described.

The proposed model provides a realistic representation of hydraulic and mechanical behavior, which is an essential requirement for numerical modeling of coupled hydro-mechanical problems. It is applied to predict the hydro-mechanical behavior of Pearl clay, speswhite kaolin and Bourke silt and thus, the ability of model has been verified.

It should be noted that, the proposed model is able to simulate the behavior of a soil sample in saturated and unsaturated conditions with a single set of material parameters. Moreover, the behavior of soils with a wide range from silts to collapsible and highly expansive clays could be simulated with unified constitutive equations.

References

[1] Sharma R. Mechanical behaviour of unsaturated highly expansive clays. PhD Dissertation, University of Oxford, UK; 1998.

[2] Alonso E, Gens A, Josa A. A constitutive model for partially saturated soils. Geotechnique 1990; 40(3): 405-430.

[3] Dangla P, Malinsky L, Coussy O. Plasticity and imbibitiondrainage curves for unsaturated soils: A unified approach. In: Proc. 6th Int. Conf. on Numerical Models in Geomechanics, Montreal, Balkema, Rotterdam, Netherlands; 1997, p. 141–146.

[4] Vaunat J, Romero E, Jommi C. An elastoplastic hydromechanical model for unsaturated soils. In: Tarantino A, Mancuso C, editors. International workshop on unsaturated soils: Experimental evidence and theoretical approaches in unsaturated soils, Balkema, Rotterdam; 2000, p. 121–138.

[5] Jommi C. Remarks on the constitutive modelling of unsaturated soils. In: Tarantino A, Mancuso C, editors. International workshop on unsaturated soils: Experimental evidence and theoretical approaches in unsaturated soils, Balkema, Rotterdam; 2000, p. 139–53.

[6] Buisson M, Wheeler S. Inclusion of hydraulic hysteresis in a new elasto-plastic framework for unsaturated soils. In: Tarantino A, Mancuso C, editors. International workshop on unsaturated soils: Experimental evidence and theoretical approaches in unsaturated soils, Balkema, Rotterdam; 2000, p. 109–19.

[7] Wheeler S, Sharma R, Buisson M. Coupling of hydraulic hysteresis and stress-strain behavior in unsaturated soils. Geotechnique 2003, 53(1): 41-53.

[8] Thu TM, Rahardjo H, Leong EC. Elastoplastic model for unsaturated soil with incorporation of the soil-water characteristic curve. Can Geotech J 2007; 44(1): 67-77.

[9] Sheng D, Sloan S, Gens A. A constitutive model for unsaturated soils: thermomechanical and computational aspects. Comput Mech 2004; 33: 453-465.

[10] Sun D, Sheng D, Sloan S. Elastoplastic modelling of hydraulic and stress–strain behaviour of unsaturated soils. Mech Mater 2007; 39: 212–221.

[11] Li XS. Thermodynamics-based constitutive framework for unsaturated soils. 1: Theory. Geotechnique 2007; 57(5): 411–422.

[12] Li XS. Thermodynamics-based constitutive framework for unsaturated soils. 2: A basic triaxial model. Geotechnique 2007; 57(5), 423–435.

[13] Khalili N, Habte M, Zargarbash S. A fully coupled flow deformation model for cyclic analysis of unsaturated soils including hydraulic and mechanical hystereses. Comput Geotech 2008; 35(6): 872-889.

[14] Della Vecchia G, Jommi C, Romero E. A fully coupled elastic–plastichydromechanical model for compacted soils accounting for clay activity. Int JNumer Anal Meth Geomech 2013;37:503–35.

[15] Mašín D. Double structure hydromechanical coupling formalism and a model forunsaturated expansive clays. Eng Geol 2013; 165: 73-88.

[16] Wong K, Mašín D. Coupled hydro-mechanical model for partially saturated soils predictingsmall strain stiffness. Comput Geotech 2014; 61: 355-369.

[17] Chiu CF, NG CWW. A state-dependent elasto-plastic model for saturated and unsaturated soils. Geotechnique 2003, 53(9): 809-829.

[18] Wheeler S, Sivakumar V. An elasto-plastic critical state framework for unsaturated soil. Geotechnique 1995; 45(1): 35-53.

[19] Cui Y, Delage P. Yielding and plastic behaviour of an unsaturated compacted silt. Geotechnique 1996; 46(2): 291-311.

[20] Georgiadis K, Potts DM, Zdravkovic L. Three-dimensional constitutive model for partially and fully saturated soils. Int J Geomech 2005; 5: 244-255.

[21] Wheeler S. Inclusion of speciefic water volume within an elasto-plastic model for unsaturated soils. Can Geotech J 1996; 33: 42-57.

[22] Sun D, Sun W, Xiang L. Effect of degree of saturation on mechanical behavior of unsaturated soils and its elastoplastic simulation. Comput Geotech 2010; 37(5): 678‑88.

[23] Muraleetharan K, Liu C, Wei C, Kibbey T, Chen L. An elastoplastic framework for coupling hydraulic and mechanical behavior of unsaturated soils. Int J Plasticity 2009; 25(3): 473-490.

[24] Ghasemzadeh H, Ghoreishian Amiri SA. A hydro-mechanical elastoplastic model for unsaturated soils under isotropic loading conditions. Comput Geotech 2013; 51: 91-100.

[25] Liu C, Muraleetharan K. Coupled hydro-mechanical elastoplastic constitutive model for unsaturated sands and silts. I: Formulation. International Journal of Geomechanics 2012; 12(3): 239-247.

[26] Liu C, Muraleetharan K. Coupled hydro-mechanical elastoplastic constitutive model for unsaturated sands and silts. II: Integration, calibration, and validation. International Journal of Geomechanics 2012; 12(3): 248-259.

[27] Wei C. Static and dynamic behavior of multiphase porous media: Governing equations and finite element implementation. PhD Dissertation, University of Oklahoma, Oklahoma; 2001.

[28] Hashiguchi K. Subloading surface model in unconventional plasticity. Int J Soilds Struct 1989; 25(8): 917-945.

[29] Hashiguchi K, Saitoh K, Okayasu T, Tsutsumi S. Evaluation of typical conventional and unconventional plasticity models for prediction of softening behaviour of soils. Geotechnique 2002; 52(8): 561–578.

[30] Dafalias Y, Popov E. A model of nonlinearly hardening materials for complex loading. Acta Mech 1975; 21: 173-192.

[31] Dafalias Y, Popov E. Plastic internal variables formalism of cyclic plasticity. ASME J Appl Mech 1976; 43: 645-651.

[32] Liu C, Muraleetharan K. Description of soil water characteristic curves using the bounding surface plasticity theory. In: 4th International Conference on Unsaturated Soils; 2006, p. 2432-2440.

[33] Feng M, Fredlund D. Hysteretic influence associated with thermal conductivity sensor measurments. In: Proceeding of from theory to the practice of unsaturayed soil mechanics, in associated with 52nd Can. Geotech. Conference and Unsaturated Soil Group, Regiana; 1999, p. 14:2:14-14:2:20.

[34] Sun D, Sheng D, Xu Y. Collapse behavior of unsaturated compacted soil with different initial densities. Can Geotech J 2007; 44: 673-686.

[35] Sivakumar V, Wheeler S. Influence of compaction procedure on the mechanical behaviour of an unsaturated compacted clay. Part 1: Wetting and isotropic compression. Geotechnique 2000; 50(4): 359-368.

[36] Wheeler S, Sivakumar V. Influence of compaction procedure on the mechanical behaviour of an unsaturated compacted clay. Part 2: Shearing and constitutive modelling. Geotechnique 2000; 50(4): 369-376.

[37] Uchaipichat A. Experimental investigation and constitutive modelling of thermo-hydro-mechanical coupling in unsaturated soils. PhD Dissertation, The University of New South Wales, Sydney; 2005.

Table 1. Model parameters for Pearl clay

Hydraulic parameters		
	b_1	23 kPa
	d_1	1.657
	b_2	105 kPa
	d_2	5.0
	Γ^e	-9000 kPa
	h	15
	g	0.1
	$n_{w_{sat}}$	0.49
	$n_{w_{res}}$	0.305
Mechanical parameters		
	F_0	235 kPa
	u	240
	λ_s	0.01
	K	0.002
	k	0.05
	υ	0.25
	m	0.93
Coupling parameters		
	α_1	0.1
	α_2	0.1

Table 2. Model parameters for speswhite kaolin

Hydraulic parameters		
	b_1	20 kPa
	d_1	2
	b_2	1135 kPa
	d_2	0.77
	Γ^e	-20000 kPa
	h	30
	g	1.5
	$n_{w_{sat}}$	0.5
	$n_{w_{res}}$	0.17
Mechanical parameters		
	F_0	235 kPa
	u	120
	λ_s	0.11
	K	0.007
	k	0.025
	υ	0.4
	m	0.9
Coupling parameters		
	α_1	1
	α_2	0.1

Table 3. Model parameters for Bourke silt

Hydraulic parameters		
	b_1	20 kPa
	d_1	2
	b_2	200 kPa
	d_2	5.5
	Γ^e	-20000 kPa
	h	30
	g	1.4
	$n_{w_{sat}}$	0.5
	$n_{w_{res}}$	0.17
Mechanical parameters		
	F_0	210 kPa
	u	150
	λ_s	0.3
	K	0.003
	k	0.002
	υ	0.25
	m	0.94
Coupling parameters		
	α_1	1
	α_2	0.1

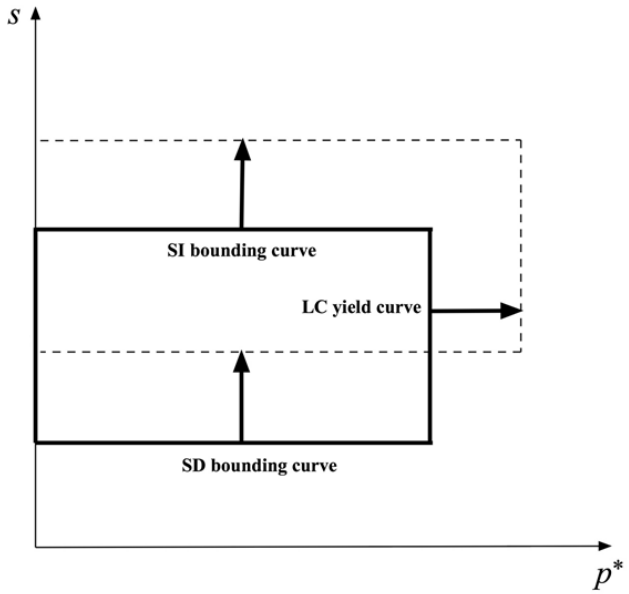

Figure 1. LC normal yield curve, SI and SD bounding curves and their evolution in $p^* - s$ space

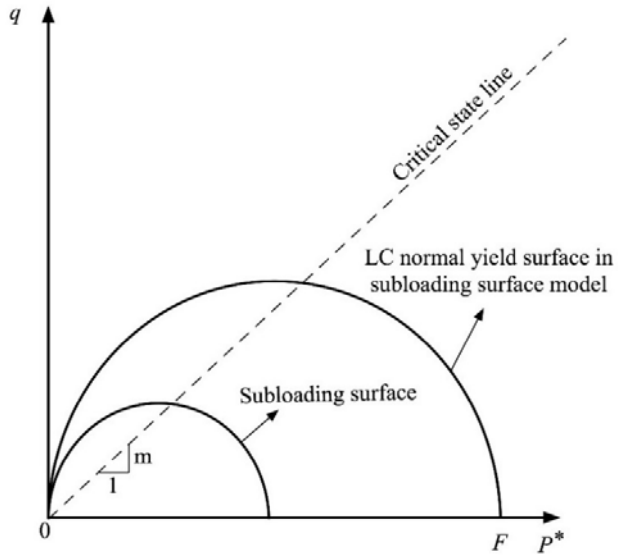

Figure 2. LC normal yield and subloading surfaces in $p^* - q$ plane

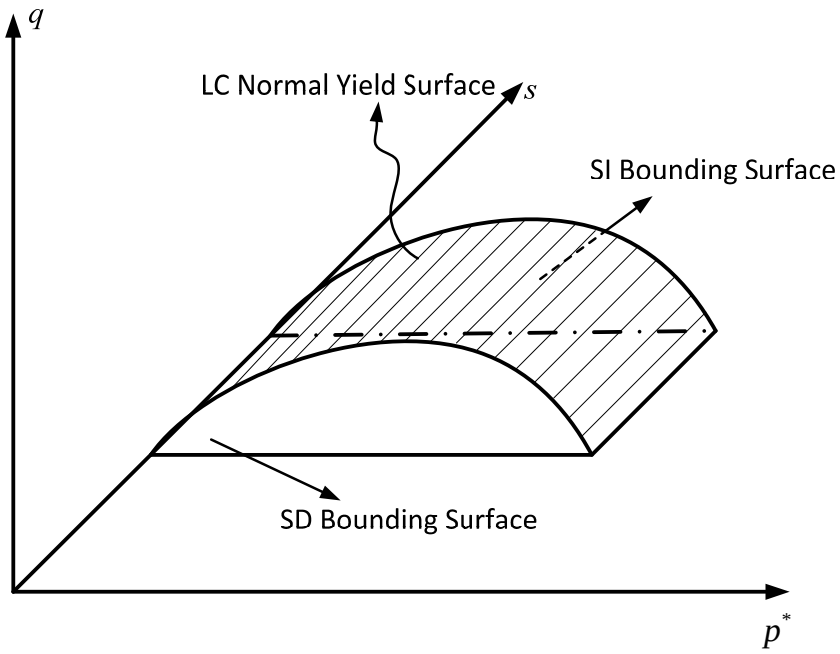

Figure 3. Yield surfaces in $q - p^* - s$ space

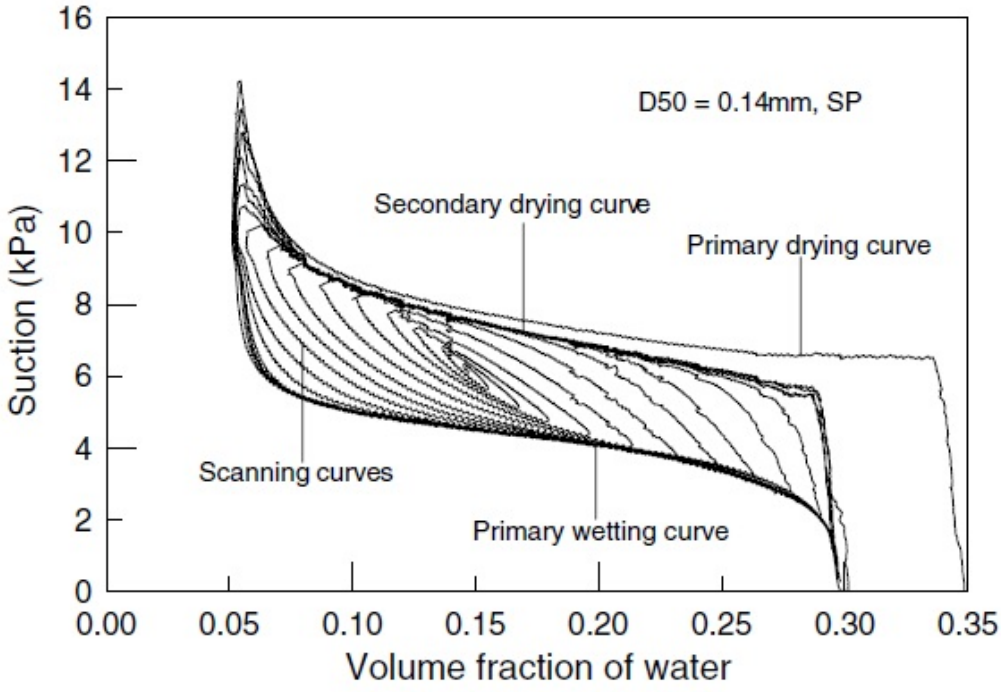

Figure 4. Example of measured SWCCs [23]

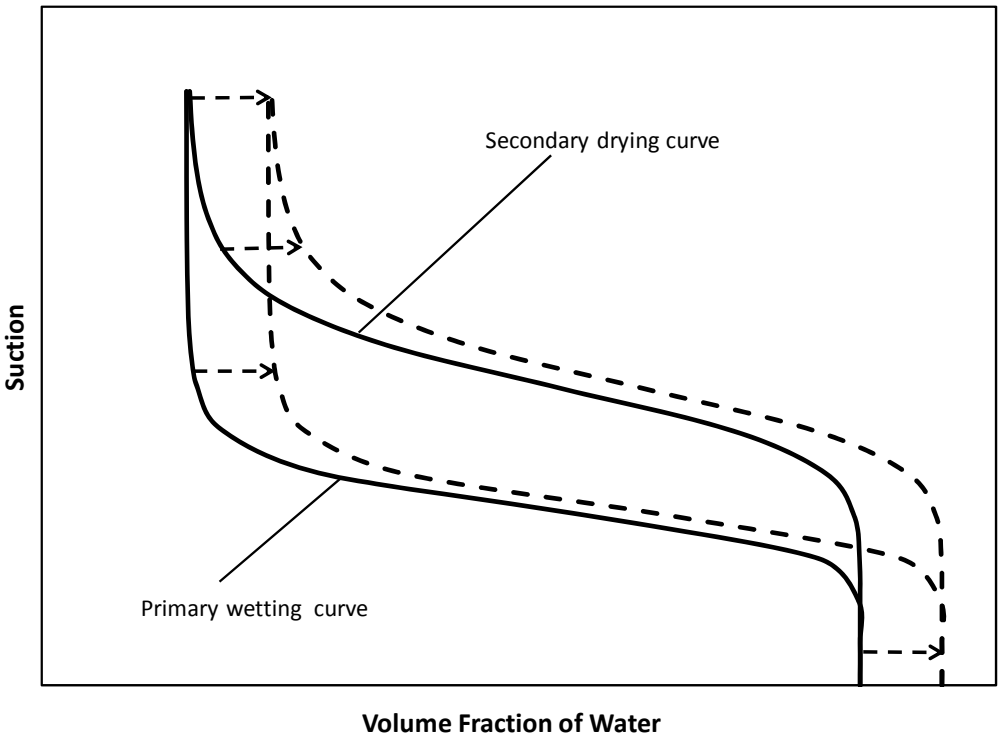

Figure 5. Movement of primary wetting and secondary drying curves due to plastic part of volumetric deformation [24]

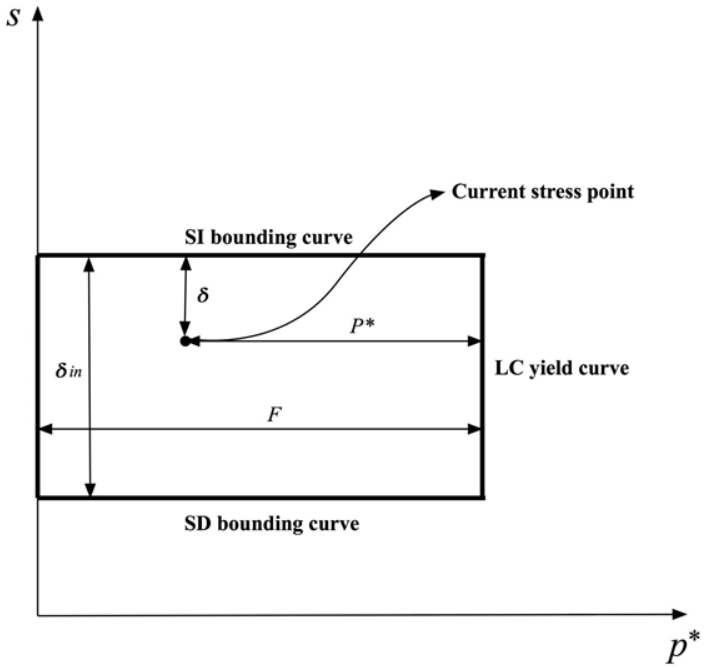

Figure 6. Graphical determination of P^*, F, δ and δ_{in}

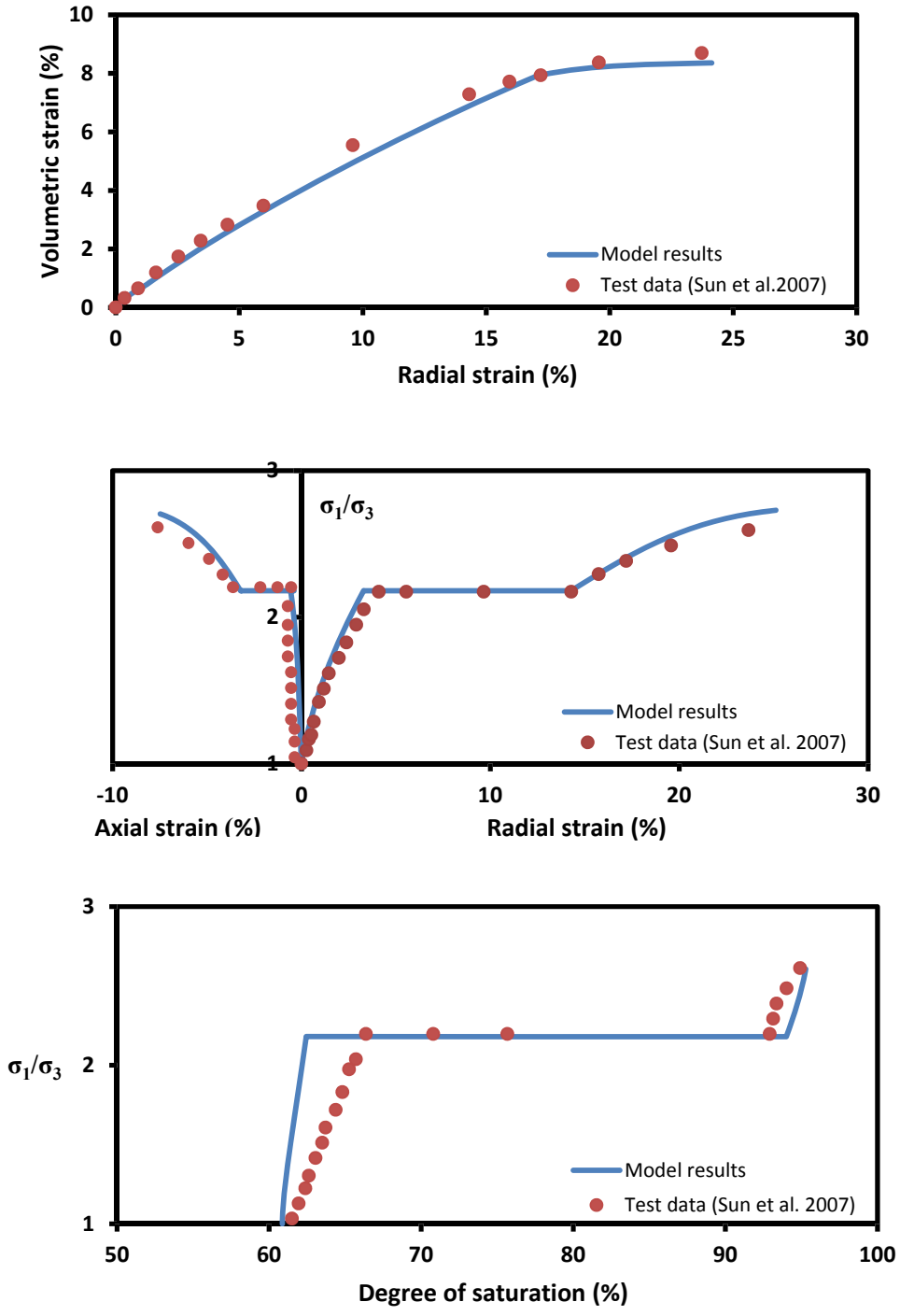

Figure 7. Comparison of predictions and experimental results for Pearl clay under triaxial extension test icluding collapse test

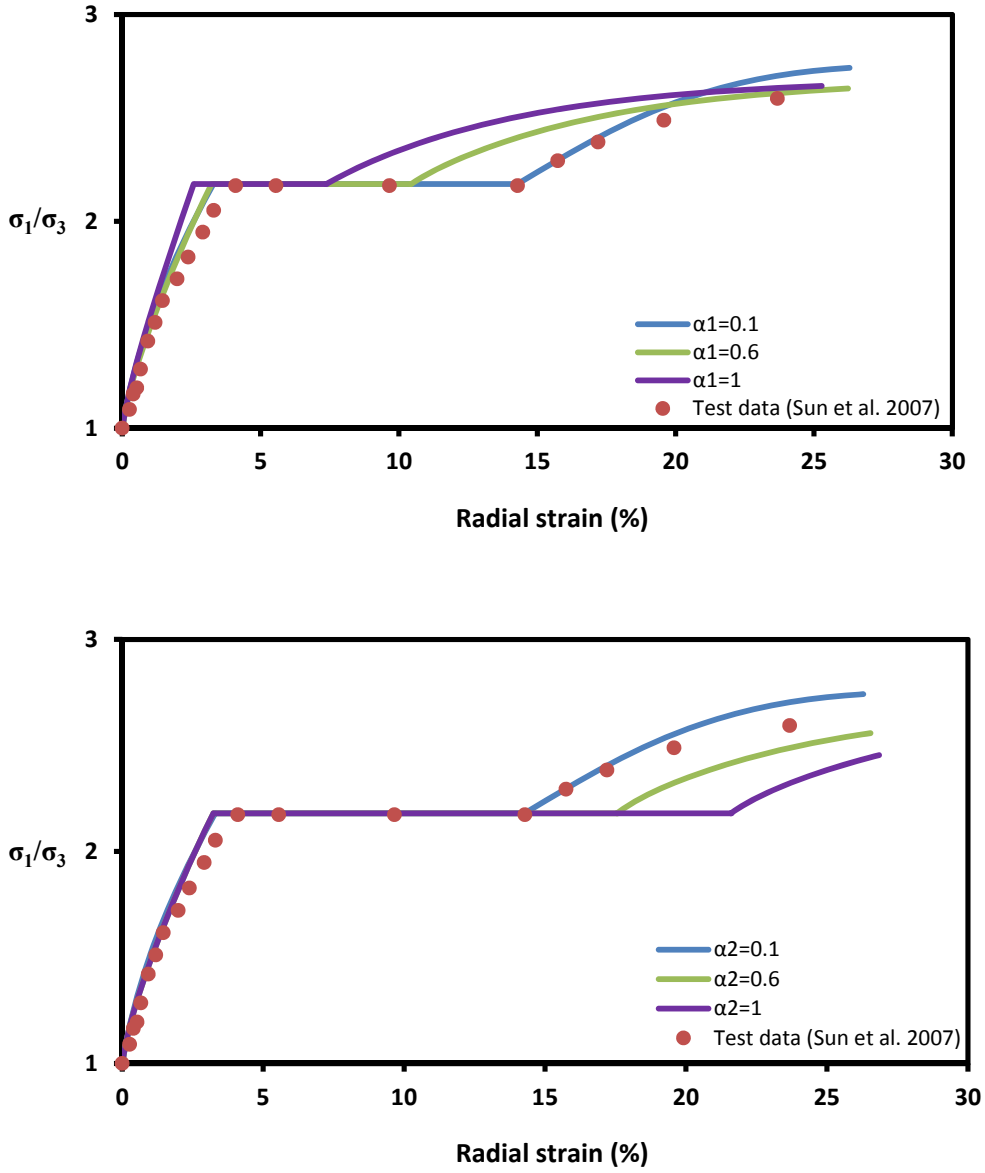

Figure 8. Sensitivity of the results to α_1 and α_2

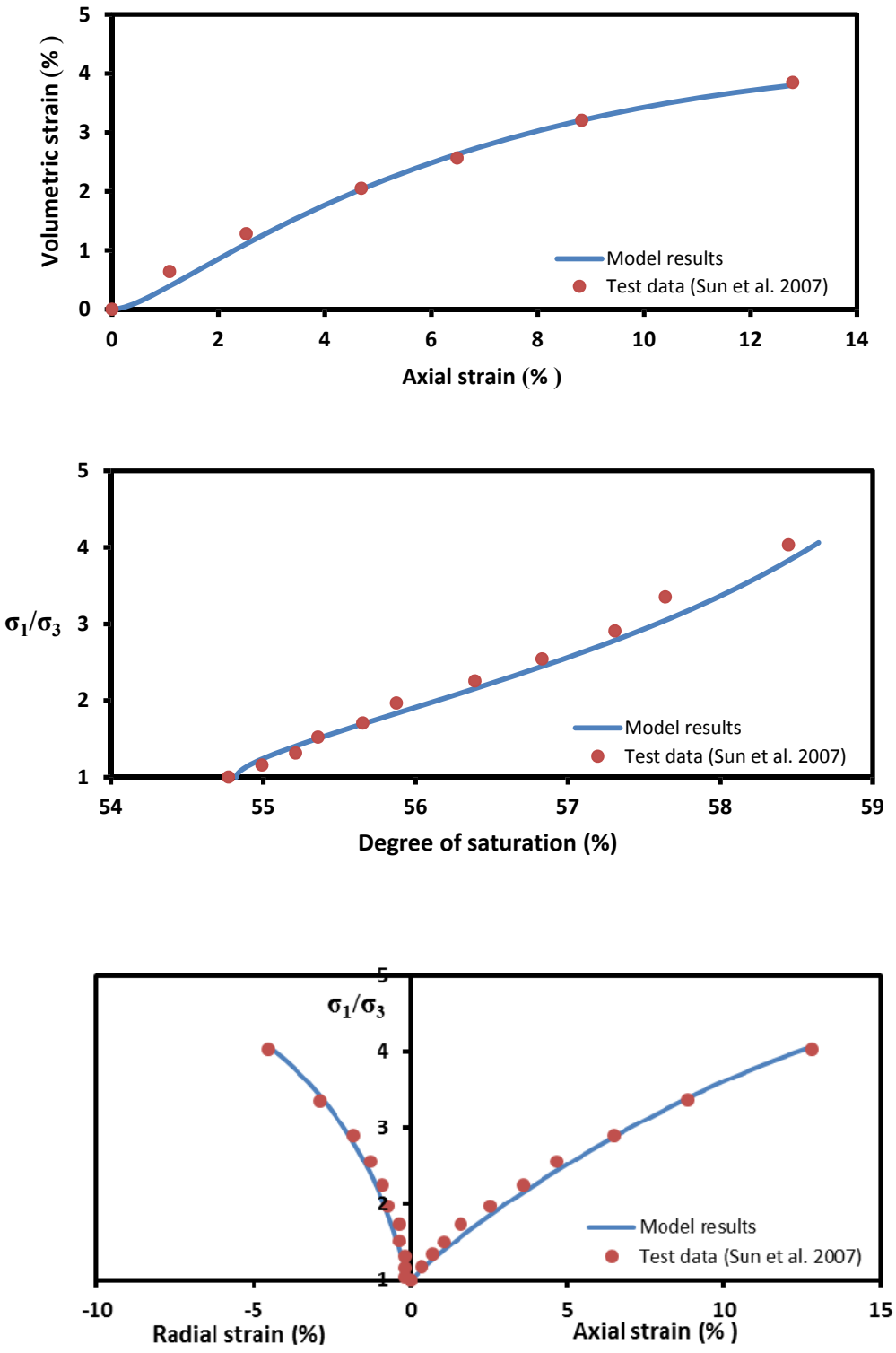

Figure 9. Comparison of predictions and experimental results for Pearl clay under triaxial loaidng test with constatnt suction and mean net stress

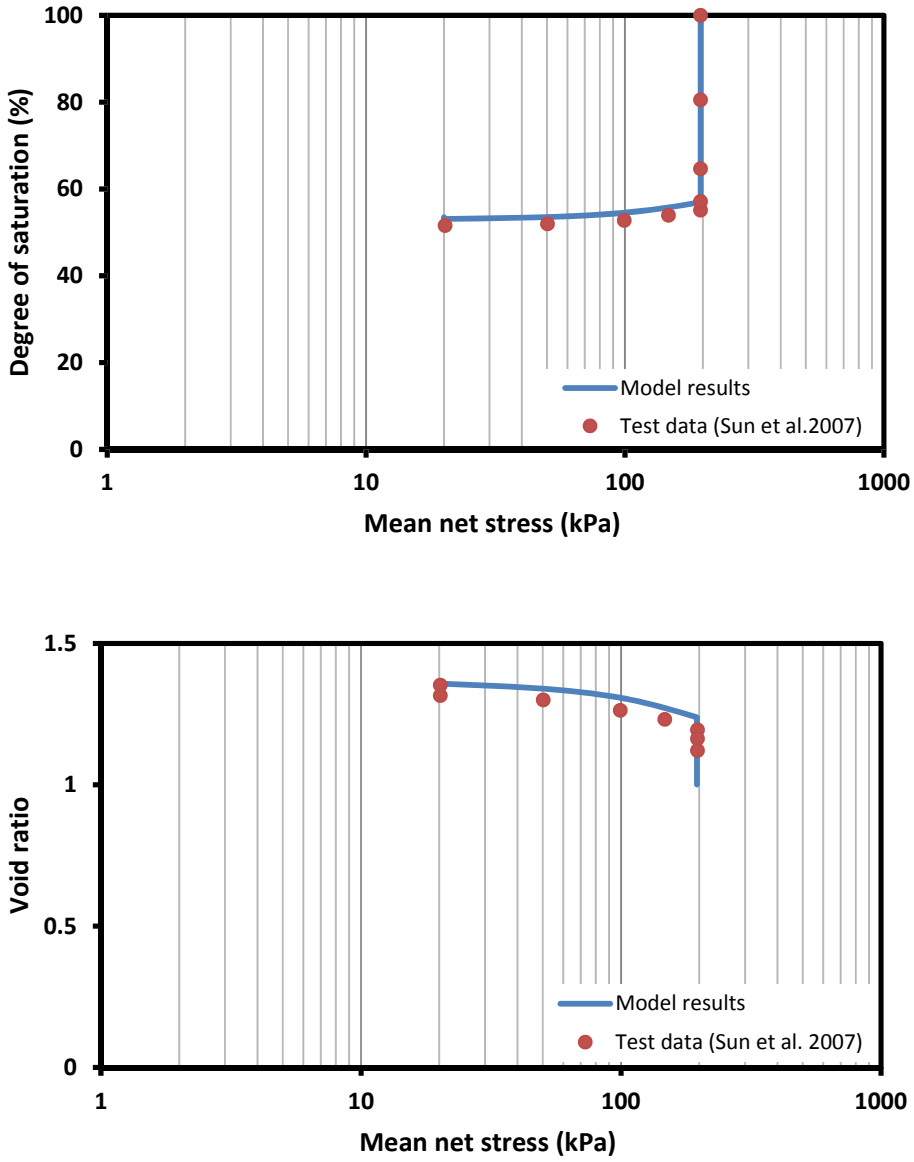

Figure 10. Comparison between the measured and predicted results of collapse test for Pearl clay (the test with three loading phases)

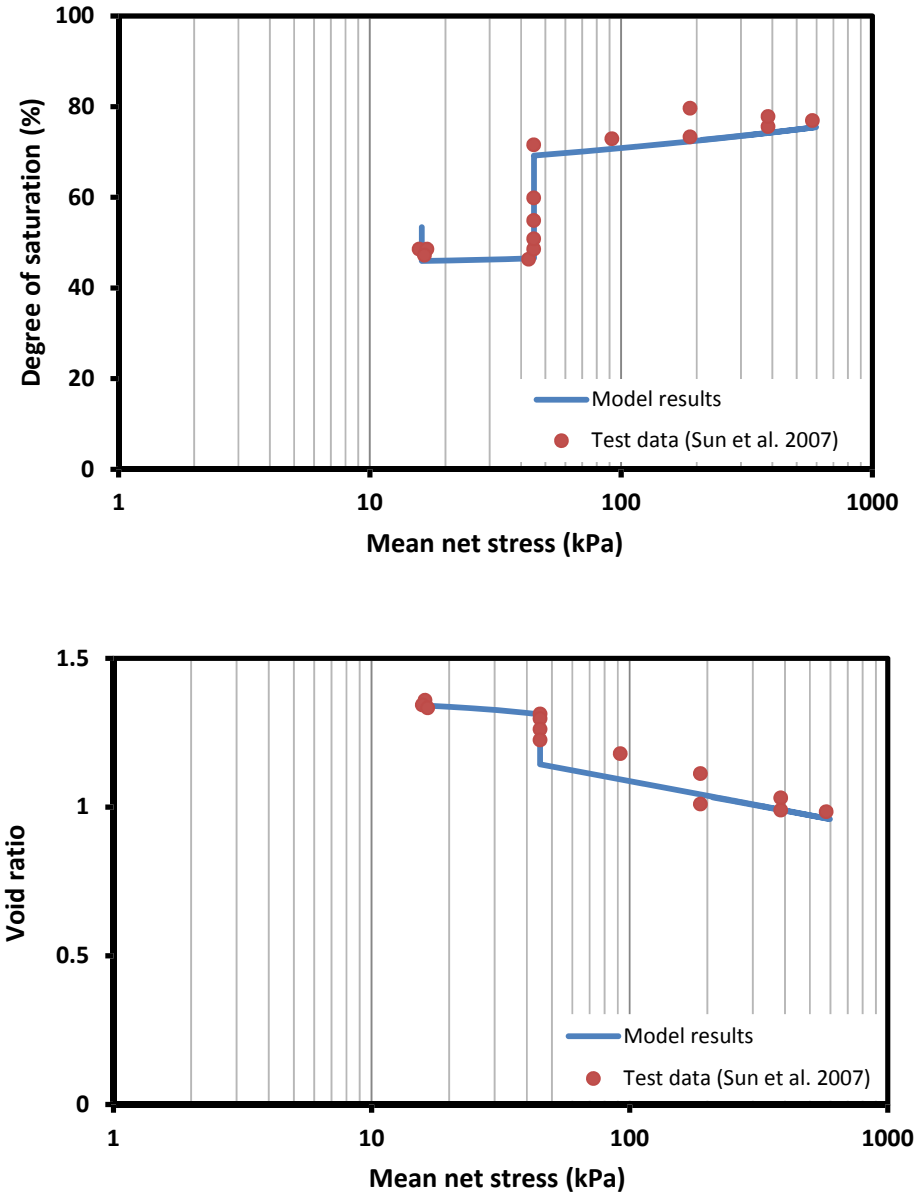

Figure 11. Comparison between the measured and predicted results of collapse test for Pearl clay (the test with five loading phases)

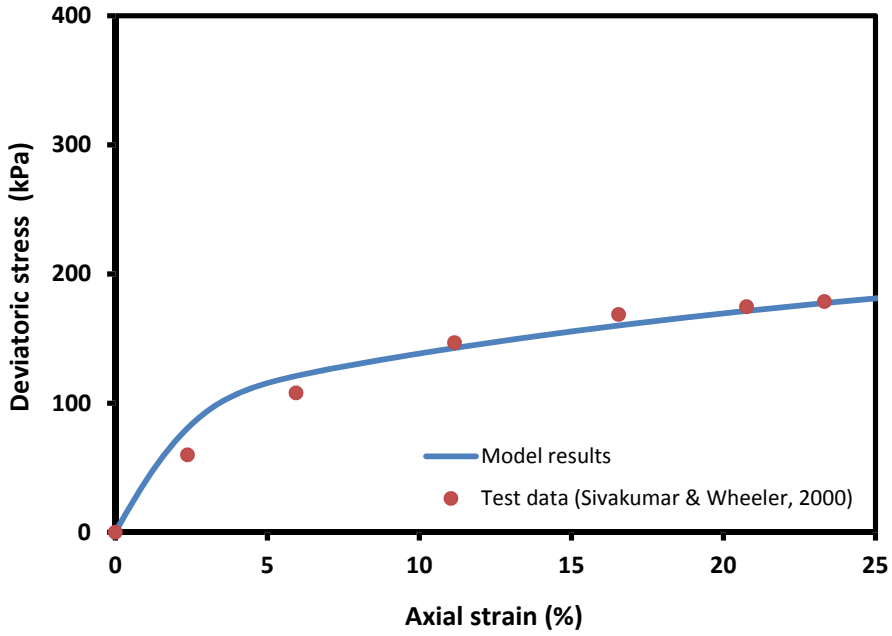

Figure 12. Comparison between the measured and calculated results for saturated speswhite kaolin under triaxial loading

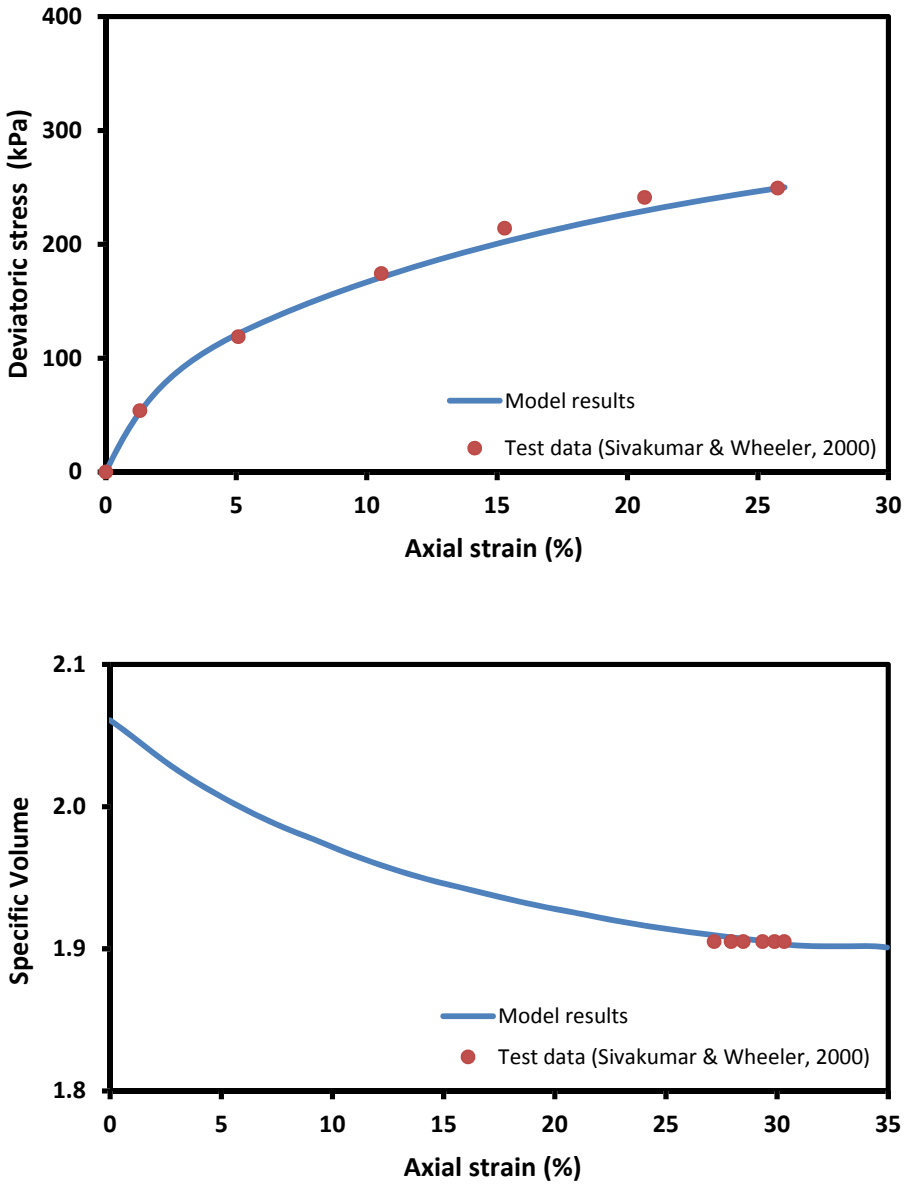

Figure 13. Comparison between the measured and calculated results for an unsaturated speswhite kaolin sample under triaxial loading ($s = 100$ kPa)

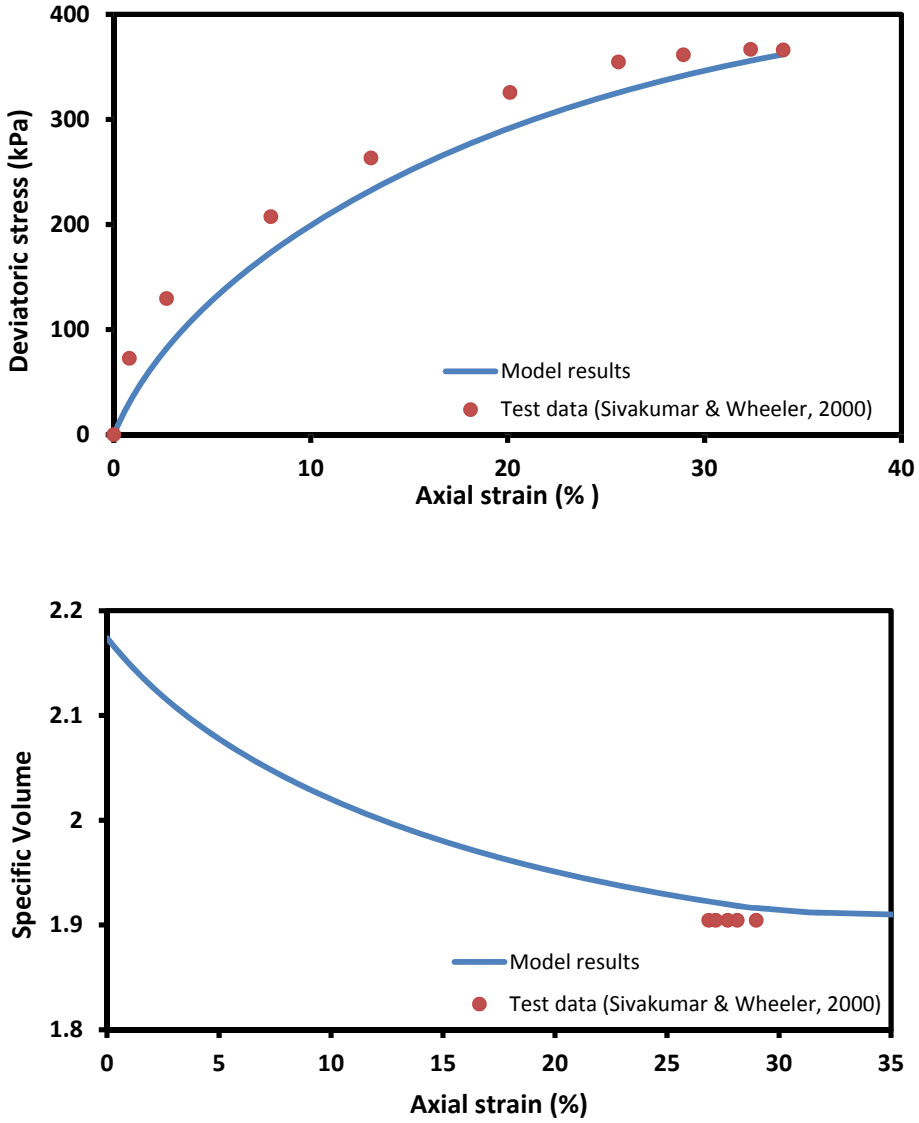

Figure 14. Comparison between the measured and calculated results for an unsaturated speswhite kaolin sample under triaxial loading ($s = 300$ kPa)

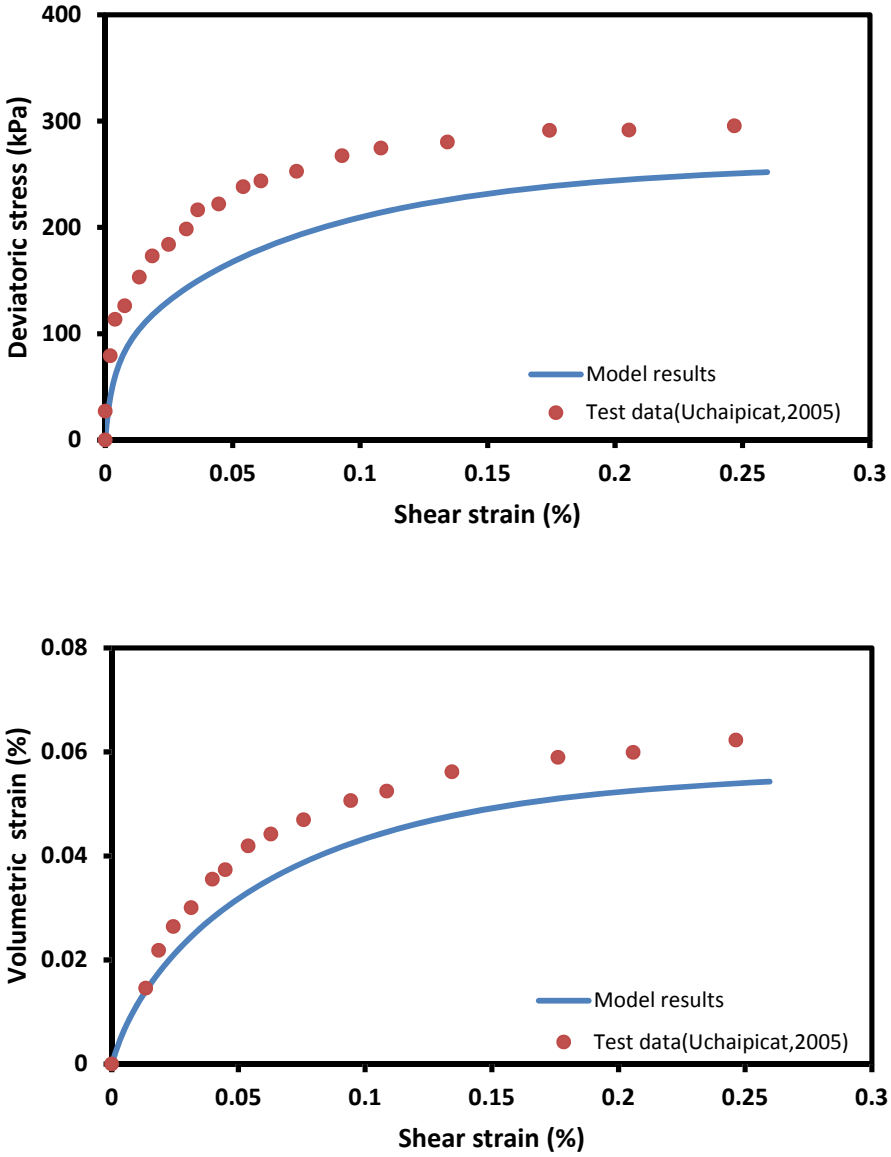

Figure 15. Comparison between the measured and calculated results for saturated Bourke silt under triaxial loading

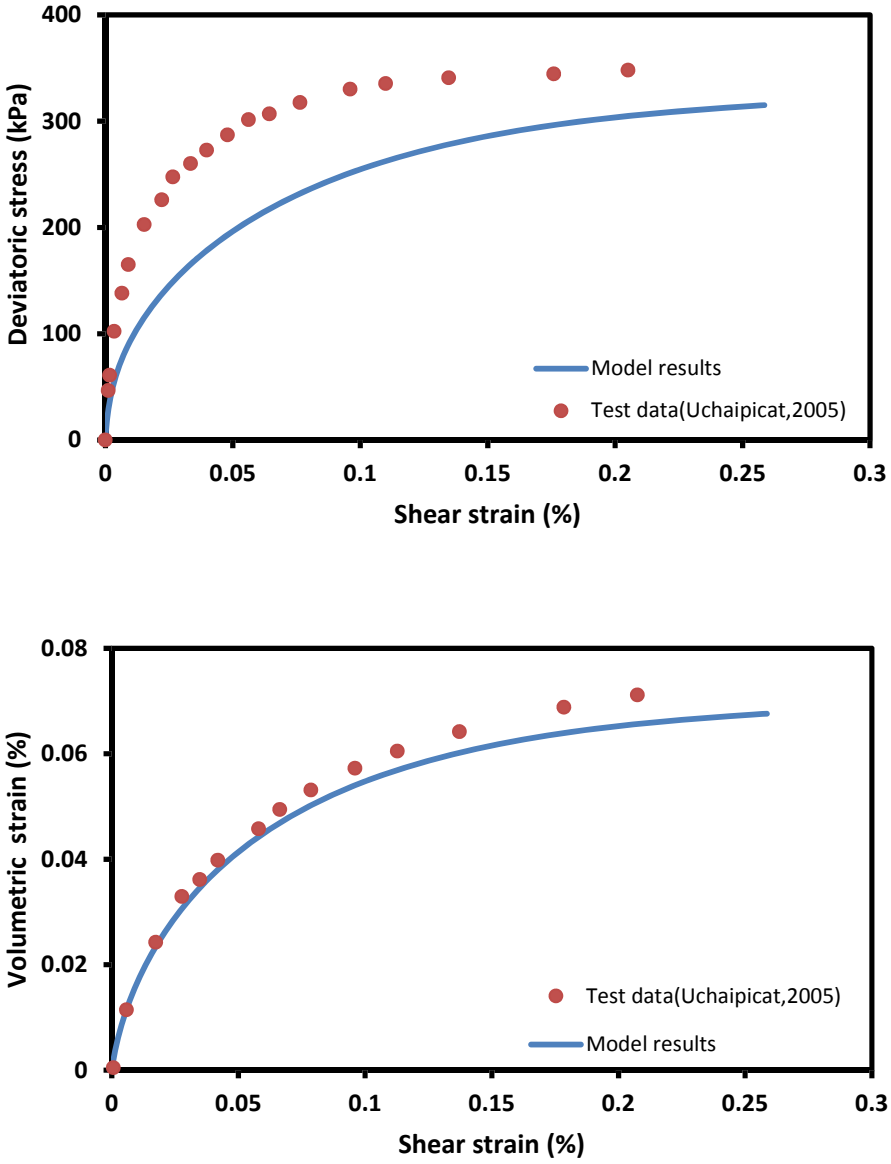

Figure 16.Comparison between the measured and calculated results for an unsaturated Bourke silt sample under triaxial loading ($s = 100$ kPa)

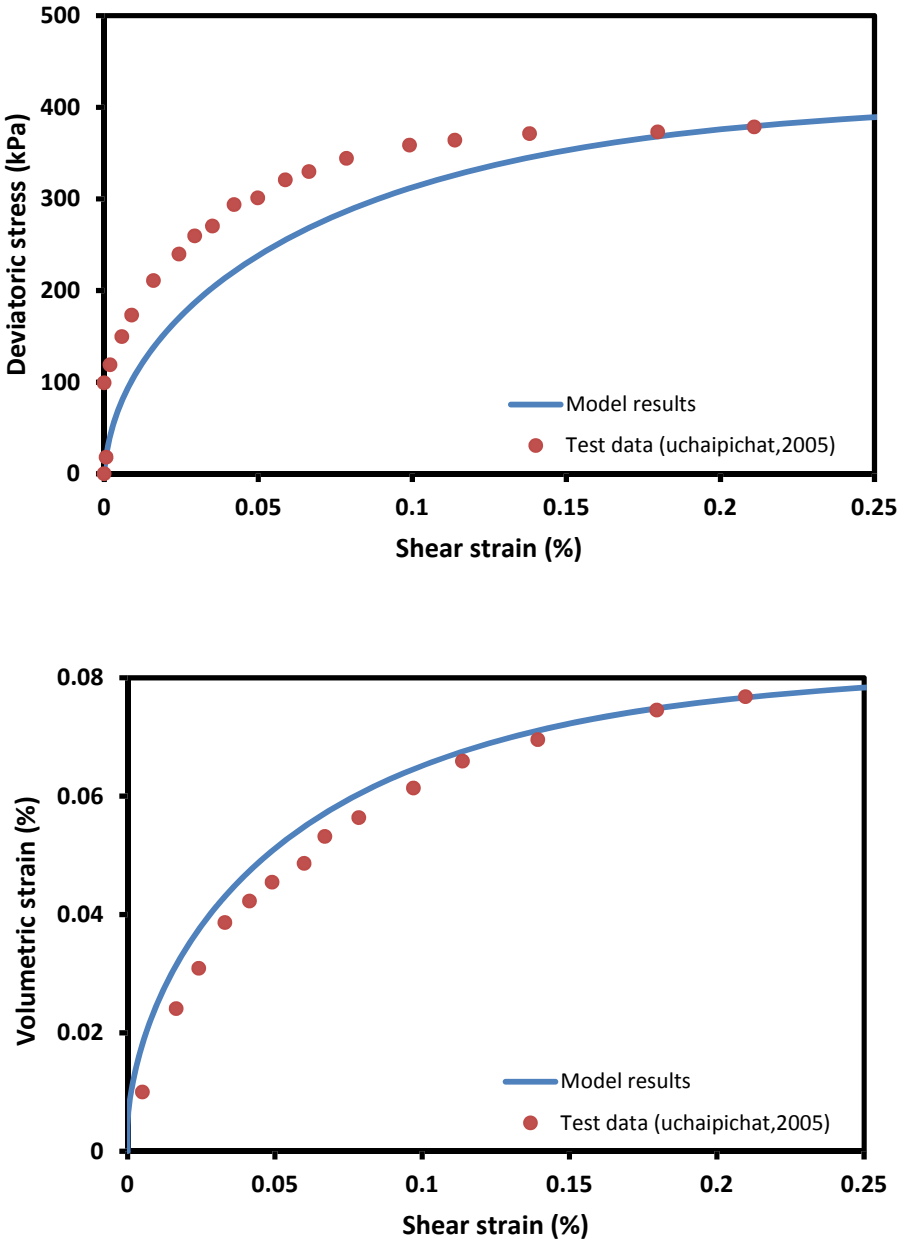

Figure 17. Comparison between the measured and calculated results for an unsaturated Bourke silt sample under triaxial loading ($s = 300$ kPa)